$Si_4I_{11}^+$ (Fig. 4(a)). The chain structure is most stable when the iodine-bridged structure is located at the center.

$Si_nI_{4n/3+3}^+$ clusters in $6 < n < 16$ region seem to have cyclic structures. Because 3- to 8-membered rings are probable structures, we have compared possible acyclic and cyclic structures (calculated for Si_9I_{18} and $Si_{10}I_{20}$), and found that the cyclic cluster with 5-membered ring is the most stable form among them. The difference between neutral and positively charged clusters is the existence of iodine-bridged structure for the latter. The optimized structure for $Si_7I_{13}^+$ with 5-membered ring (Fig. 4(b)) consists of the 5-membered ring (silicons 1–5) and the iodine-bridged structure (silicons 1, 5, and 6). At $n = 8$, 11, and 14, bi-, tri-, and tetra-cyclic clusters are formed with elimination of iodine. This leads to lower ratio of iodine to silicon in $6 < n < 16$ region than in $n < 7$ region.

The clusters in $n \geq 16$ region form cages. For an example, the optimized cage cluster of $Si_{16}I_{17}^+$ composed of eight 5-membered rings (envelop form) and one 6-membered ring (boat form; silicons 1–6) is shown in Figure 4(c).

4. CONCLUSION

Both positively and negatively charged silicon subiodide clusters obtained by the laser ablation of bulk powder silicone tetraiodide have been investigated by time-of-flight mass spectroscopy and *ab initio* calculations for their structures have been performed. A tendency to form chain, ring, and cage structures for $n \leq 6$, $6 < n < 16$, and $n \geq 16$, respectively, has been found experimentally and confirmed by the calculations. These iodine terminated structures are similar to the hydrogen terminated clusters.[1,2] Therefore iodine can be used for silicon cluster termination as an alternative to hydrogen. Furthermore, iodine termination may allow better cluster surface modification than hydrogen termination due to the difference in the strength of their bonds to silicon.

Acknowledgments: This work is partially supported by Program Research, Center for Interdisciplinary Research, Tohoku University.

References and Notes

1. G. Rechtsteiner, O. Hampe, and M. Jarrold, *J. Phys. Chem. B* 105, 4188 (2001).
2. Ch. Hollenstein, W. Schwarzenbach, A. A. Howling, C. Courteille, J.-L. Dorier, and L. Sansonnens, *J. Vac. Sci. Technol. A* 14, 535 (1996).
3. S. Izumi, N. Hayafuji, K. Ito, K. Sato, and M. Otsubo, *Appl. Phys. Lett.* 68, 3102 (1996).
4. M. J. Frisch, G. W. Trucks, H. B. Schlegel, G. E. Scuseria, M. A. Robb, J. R. Cheeseman, J. A. Montgomery, Jr., T. Vreven, K. N. Kudin, J. C. Burant, J. M. Millam, S. S. Iyengar, J. Tomasi, V. Barone, B. Mennucci, M. Cossi, G. Scalmani, N. Rega, G. A. Petersson, H. Nakatsuji, M. Hada, M. Ehara, K. Toyota, R. Fukuda, J. Hasegawa, M. Ishida, T. Nakajima, Y. Honda, O. Kitao, H. Nakai, M. Klene, X. Li, J. E. Knox, H. P. Hratchian, J. B. Cross, C. Adamo, J. Jaramillo, R. Gomperts, R. E. Stratmann, O. Yazyev, A. J. Austin, R. Cammi, C. Pomelli, J. W. Ochterski, P. Y. Ayala, K. Morokuma, G. A. Voth, P. Salvador, J. J. Dannenberg, V. G. Zakrzewski, S. Dapprich, A. D. Daniels, M. C. Strain, O. Farkas, D. K. Malick, A. D. Rabuck, K. Raghavachari, J. B. Foresman, J. V. Ortiz, Q. Cui, A. G. Baboul, S. Clifford, J. Cioslowski, B. B. Stefanov, G. Liu, A. Liashenko, P. Piskorz, I. Komaromi, R. L. Martin, D. J. Fox, T. Keith, M. A. Al-Laham, C. Y. Peng, A. Nanayakkara, M. Challacombe, P. M. W. Gill, B. Johnson, W. Chen, M. W. Wong, C. Gonzalez, and J. A. Pople, *Gaussian 03, Revision B.04*, Gaussian, Inc., Pittsburgh, PA (2003).

Received: 4 May 2007. Revised/Accepted: 23 May 2007.

Biomed Microdevices (2008) 10:153–167
DOI 10.1007/s10544-007-9121-z

In vitro blood flow in a rectangular PDMS microchannel: experimental observations using a confocal micro-PIV system

Rui Lima · Shigeo Wada · Shuji Tanaka · Motohiro Takeda · Takuji Ishikawa · Ken-ichi Tsubota · Yohsuke Imai · Takami Yamaguchi

Published online: 18 September 2007

Abstract Progress in microfabricated technologies has attracted the attention of researchers in several areas, including microcirculation. Microfluidic devices are expected to provide powerful tools not only to better understand the biophysical behavior of blood flow in microvessels, but also for disease diagnosis. Such microfluidic devices for biomedical applications must be compatible with state-of-the-art flow measuring techniques, such as confocal microparticle image velocimetry (PIV). This confocal system has the ability to not only quantify flow patterns inside microchannels with high spatial and temporal resolution, but can also be used to obtain velocity measurements for several optically sectioned images along the depth of the microchannel. In this study, we investigated the ability to obtain velocity measurements using physiological saline (PS) and *in vitro* blood in a rectangular polydimethysiloxane (PDMS) microchannel (300 μm wide, 45 μm deep) using a confocal micro-PIV system. Applying this combination, measurements of trace particles seeded in the flow were performed for both fluids at a constant flow rate (Re = 0.02). Velocity profiles were acquired by successive measurements at different depth positions to obtain three-dimensional (3-D) information on the behavior of both fluid flows. Generally, the velocity profiles were found to be markedly blunt in the central region, mainly due to the low aspect ratio (h/w = 0.15) of the rectangular microchannel. Predictions using a theoretical model for the rectangular microchannel corresponded quite well with the experimental micro-PIV results for the PS fluid. However, for the *in vitro*

R. Lima · M. Takeda · T. Ishikawa · K.-i. Tsubota · Y. Imai · T. Yamaguchi
Department of Bioengineering and Robotics,
Graduate School of Engineering, Tohoku University,
6-6-01 Aoba,
980-8579 Sendai, Japan

R. Lima
Department of Mechanical Tech, ESTiG, Braganca Polyt.,
C. Sta. Apolonia,
5301-857 Braganca, Portugal

S. Wada
Department of Mechanical Science and Bioengineering,
Graduate School of Engineering Science, Osaka University,
Toyonaka 560-8531 Osaka, Japan

S. Tanaka
Department of Nanomechanics, Graduate School of Engineering,
Tohoku University,
6-6-01 Aoba,
980-8579 Sendai, Japan

M. Takeda
Division of Surgical Oncology, Graduate School of Medicine,
Tohoku University,
2-1 Seiryo-machi, Aoba-ku,
980-8575 Sendai, Japan

R. Lima (✉)
Yamaguchi and Ishikawa Lab. (PFSL), Department of Bioengineering and Robotics, Graduate School of Engineering,
Tohoku University,
6-6-01 Aoba,
980-8579 Sendai, Japan
e-mail: rui@pfsl.mech.tohoku.ac.jp

blood with 20% hematocrit, small fluctuations were found in the velocity profiles. The present study clearly shows that confocal micro-PIV can be effectively integrated with a PDMS microchannel and used to obtain blood velocity profiles along the full depth of the microchannel because of its unique 3-D optical sectioning ability. Advantages and disadvantages of PDMS microchannels over glass capillaries are also discussed.

Keywords Microcirculation · Confocal micro-PIV · PDMS microchannel · Red blood cells · Mesoscopic blood flow

1 Introduction

Blood is not a homogeneous fluid, but one composed mainly of a suspension of red blood cells (RBCs) in plasma. In addition, the non-continuum behavior of blood flow through microvessels leads to complex flow mechanics, which are not yet clearly understood (Goldsmith and Turitto 1986; Secomb 1995; Mchedlishvili and Maeda 2001). Because several important physiological and pathological phenomena occur in the microcirculation, velocity profiles have been intensively studied both *in vivo* (Einav et al. 1975; Tangelder et al. 1986; Golster et al. 1999; Parthasarathi et al. 1999; Nakano et al. 2003) and *in vitro* (Gaehtgens et al. 1970; Baker and Wayland 1974; Born et al. 1978; Cochrane et al. 1981; Gaehtgens 1987; Uijttewaal et al. 1994; Alonso et al. 1995; Moger et al. 2004; Kim and Lee 2006; Lima et al. 2007) using several blood flow measuring techniques. Both *in vivo* and *in vitro* experiments have played important roles in our understanding of several phenomena in the microcirculation. Although several comprehensive reviews about blood flow behavior in microvessels have been published (Caro et al. 1978; Chien et al. 1984; Secomb 1995; Mchedlishvili and Maeda 2001; Pries and Secomb 2003), much remains unknown about physiological and pathological phenomena occurring in the microcirculation.

Historically, the most commonly used experimental techniques to study blood flow in the microcirculation have been double-slit photometry (Gaehtgens et al. 1970; Baker and Wayland 1974), video microscopy and image analysis (Bugliarello et al. 1963; Tangelder et al. 1986; Goldsmith and Turitto 1986; Gaehtgens 1987; Alonso et al. 1995; Parthasarathi et al. 1999; Tsukada et al. 2000), and laser-Doppler anemometry (Einav et al. 1975; Born et al. 1978; Cochrane et al. 1981; Uijttewaal et al. 1994; Golster et al. 1999). However, with these techniques, both spatial resolution and velocity accuracy are unsatisfactory.

In recent years, because of advances in computers, optics, and digital image processing techniques, it has become possible to combine a conventional particle image velocimetry (PIV) system (Adrian 1991; Raffel et al. 1998) with an inverted epifluorescent microscope (Santiago et al. 1998; Koutsiaris et al. 1999). As a result, this combination, known as a micro-PIV, has greatly increased the resolution of conventional PIV. Because of the success of micro-PIV in measuring accurate velocity fields of homogeneous fluids in microfluidic devices (Nguyen and Wereley 2002), the technique has been recently used to investigate blood flow behavior in both microchannels and microvessels (Nakano et al. 2003; Bitsch et al. 2005; Vennemann et al. 2006).

Although the conventional PIV technique has proven useful in measuring blood flow velocities in microvessels, the entire flow field is illuminated and consequently the out-of-focus emitted light can result in high levels of background noise, which degrades the measured velocity fields (Meinhart et al. 2000; Nguyen and Wereley 2002). One way to minimize the depth-of-focus effect is using a confocal micro-PIV (Tanaani et al. 2002; Kinoshita et al. 2005; Lima et al. 2005, 2006) or confocal laser scanning microscopy (CLSM) micro-PIV (Park et al. 2004, 2006). This technique combines the conventional PIV system with a spinning disk confocal microscope (SDCM), which has the ability to obtain in-focus images with an optical thickness less than 1 μm (optical sectioning effect). Park et al. (2004, 2006) compared confocal micro-PIV with conventional micro-PIV and demonstrated that the former had improved particle image contrast and definition, allowing more accurate velocity measurements (see Table 1). As a result, by combining SDCM with a conventional PIV system, it is possible to achieve a PIV system with high spatial resolution able to generate velocity profiles at several optically sectioned planes along the microchannel depth.

Progress in microfabricated technologies has attracted the attention of the biomedical research community to the development of diagnostic, microfluidic devices (so-called bio-micro-electromechanical systems or a lab-on-a-chip; Sutton et al. 1997; Gomez et al. 2001; Beebe et al. 2002; Gifford et al. 2003; Minas et al. 2004; Toner and Irimia

Table 1 The lateral and axial resolutions of both conventional and confocal microscopes and optical slice thickness of confocal microscopes (Willhelm et al. 2003; Park et al. 2004)

Optical resolutions	Conventional microscopy		Confocal microscopy (SDCM)	
	40×	10×	40×	10×
Lateral resolution (μm)	0.418	1.047	0.331	0.829
Axial resolution (μm)	1.831	11.444	1.268	9.323
Optical slice thickness (μm)	Not definable		2.820	26.701

2005; Faivre et al. 2006) capable of providing useful information about the general health status of patients. However, most of the information provided by blood analysis in microchannels is based on conventional visual observations on the area and volume of the RBCs (Sutton et al. 1997; Gifford et al. 2003). We believe that the acquisition of quantitative blood flow measurements may also provide relevant information for the diagnosis of disease and the treatment of patients.

Recently, we demonstrated the ability of the confocal micro-PIV to measure both pure water and diluted suspensions of blood cells in a glass square microchannel (Lima et al. 2006); however, glass microchannels are not ideal for the study of flow properties of blood at the microscopic level, primarily because of fabrication issues and physicochemical factors (Maeda 1996). First, glass-to-glass sealing is difficult because direct bonding needs extremely smooth and flat surfaces, and indirect bonding fills the channels with adhesives, sols, and metals. Second, the fabrication of microchannels in glass is limited in depth and width because glass is isotropically etched by hydrofluoric acid using a metal mask, which has a limited durability against the etchant. Moreover, the most suitable objective lenses for the confocal micro-PIV system have limited working distances (up to 0.5 mm), which requires special considerations in microchannel design. In addition to the fabrication limitations, several physical and biochemical factors contribute to the flow behavior of blood cells through microvessels. Glass microchannels differ from microvessels in several ways: the wall is not elastic, the flow channel is often straight and long, and the inner surface does not accommodate living endothelial cells. Hence, the results from classical *in vitro* experiments (Chien et al. 1984; Pries and Secomb 2003) that used glass microchannels need to be reexamined in the light of more sophisticated microchannels, such as polydimethysiloxane (PDMS) microchannels.

Because of these limitations with glass microchannels, it is important to develop a microfluidic device more closely representative of the *in vivo* microvascular environment using a reliable microfabrication technique compatible with the state-of-the-art flow measuring techniques, such as a confocal micro-PIV system. Using a soft lithography technique, it is possible to generate extremely precise, reproducible, and versatile rectangular microchannels. Although rectangular microchannels may not be the best models to simulate the geometry of microvessels *in vivo*, many aspects of blood flow behavior through this kind of microchannel are similar to those in living microvessels (Beebe et al. 2002; Shevkoplyas et al. 2003; Toner and Irimia 2005; Faivre et al. 2006). Furthermore, experiments with this kind of microchannel enable not only precise control of experimental parameters, but also accurate measurements. Thus, it is important to examine the applicability of the confocal micro-PIV system to measure both physiological saline (PS) and *in vitro* blood with a hematocrit (~20% Hct) close to that *in vivo* in PDMS microchannels. To our knowledge, no confocal micro-PIV measurements of PS and *in vitro* blood flow in a rectangular PDMS microchannel have been published. Thus, as a first step toward integrating a confocal micro-PIV with a PDMS microchannel, measurements were first performed in a simple, straight, rectangular microchannel.

In this study, we investigated the ability of our confocal micro-PIV system to measure the velocity profiles of physiological saline (PS) and *in vitro* blood at a normal Hct in a rectangular (300 μm wide, 45 μm deep) PDMS microchannel, fabricated by soft lithography. In particular, we compared the behavior of PS and *in vitro* blood flow (20% Hct) in a rectangular microchannel with a low aspect ratio. The results presented are also a verification as to the applicability of the confocal micro-PIV to obtain detailed measurements of blood flow with Hcts similar to those encountered in microvessels.

2 Materials and methods

2.1 Fabrication of the PDMS microchannel

PDMS polymers have many useful properties, including good optical transparency and biocompatibility, easily reversible sealing to glass, elasticity, replication of fine and complex geometries, permeability to gases, thermal stability, and low cost (Duffy et al. 1998; Chang et al. 2003; Mata et al. 2005; Kaji et al. 2006). Because of these properties, this material was suitable for studying several phenomena in the microcirculation by combining it with our confocal micro-PIV system.

The PDMS rectangular microchannel was developed using a soft lithographic technique. A detailed description of the fabrication process can be found elsewhere (Lima 2007). In brief, the photomask was first created using a pattern generator (Nihon Seiko, Japan) and then a solid master was fabricated on a glass substrate with an ultrathick photoresist (SU-8 50; Kayaku MicroChem, Japan). Metal wire posts were placed on the SU-8 mold master to create the connection channels to the input/output ports. The PDMS prepolymer was prepared by mixing a commercial prepolymer and catalyzer (Silpot 184; Dow Corning, USA) at a weight ratio of 10:1. After the mixture was degassed under vacuum, the PDMS was poured into the mold master and cured by baking for about 2h at 70°C. Both master and PDMS were cooled to room temperature and the PDMS was peeled from the master. The embedded metal wire posts were then pulled out of the PDMS. Finally, the PDMS was washed with ethanol and brought into contact with a clean glass, where a reversible seal formed spontaneously.

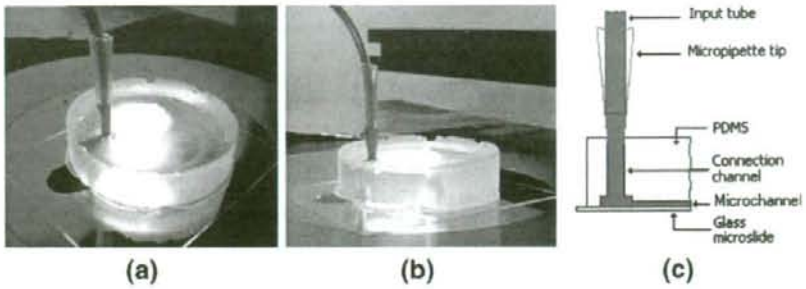

Fig. 1 PDMS microdevice with the input port (**a**) top view, (**b**) lateral view, (**c**) schematic drawing of the cross section

For this study, we found no need to make the PDMS hydrophilic by use of an oxygen plasma treatment.

The input/output ports were made by means of a 200-μl micropipette tip. This tip was inserted tightly into the connection channels where it exerted pressure on the PDMS and provided a liquid-proof seal. Top tubes (2.1 mm outer diameter, 1.1 mm inner diameter) were also fitted tightly into the micropipette to deliver the working fluids from the syringe pump (see Fig. 1). Due to the conical shape of the tip and low flow rates, we did not observe fluid leakage during our experiments. Thus, we found no need to use additional bounding adhesives, to avoid possible leakage from the microdevice.

To evaluate the performance of the confocal micro-PIV system by comparing experimental data with a theoretical model, it is important to both qualitatively and quantitatively verify the actual final geometry of the PDMS microchannel. Thus, the depth profile of the microchannel was carefully measured using a surface profiler (P-10; KLA Tencor, USA). Figure 2 shows the average depth from eight different measurements along the PDMS microchannel. The average depth was found to be 45 ± 1 μm. In addition, under a wide-field microscope, the average width was found to be 300 ± 2 μm. Thus, the measurement uncertainties for the depth and width of the microchannel were 2.2 and 0.7%, respectively. We also cut the PDMS microchannel transversely to measure the angle of the microchannel wall. We verified that the microchannel had a cross section that was nearly a perfect rectangular shape (300 μm wide, 45 μm deep). Figure 3 shows the cross section of the rectangular PDMS microchannel under an optical microscope.

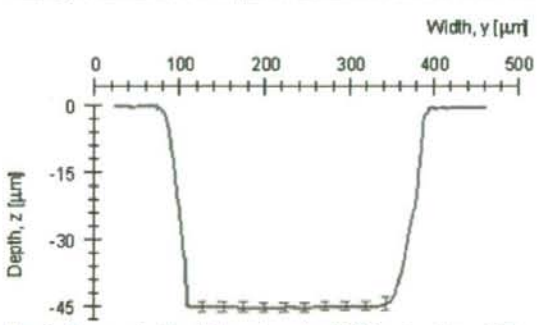

Fig. 2 Average depth of the rectangular PDMS microchannel. The measured values of the depth are expressed as the means ± standard deviation

2.2 Sample preparation: working fluids and blood samples

Two working fluids were used in this study: physiological saline (PS) and *in vitro* blood [PS containing ~20% (by volume) human red blood cells (RBCs)]. Fluids were seeded with 0.15% (*v/v*) 1-μm-diameter red fluorescent solid polymer microspheres (R0100; Duke Scientific, USA). For the *in vitro* blood, the fluorescent particles were first washed twice before seeding into the blood cell suspension.

Venous blood (~20 ml) was collected from a healthy, adult volunteer (aged 32years old) to make six samples with ~20% (by volume) RBCs suspended in PS. To prevent coagulation of the blood cells during the experiment, ethylenediaminetetraacetic acid (EDTA) was added to the glass tube. The RBCs were separated from bulk blood by centrifugation (3,000 rpm, 5 min) and aspiration of the plasma and buffy coat, and were then washed twice with PS. The washed RBCs were diluted with PS to make up the required RBC concentration by volume. The hematocrit of the RBC suspension was about ~20% (20% Hct) and the volume of each sample was 500 μl. Blood samples were stored at 4°C until the experiment was performed at room

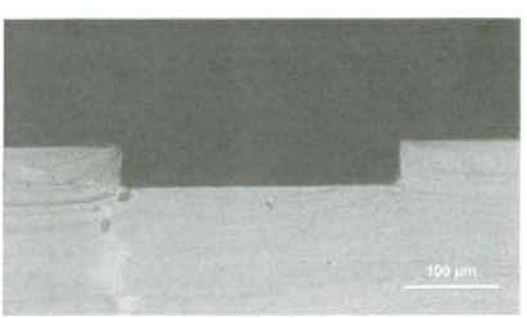

Fig. 3 Cross section of the PDMS microchannel

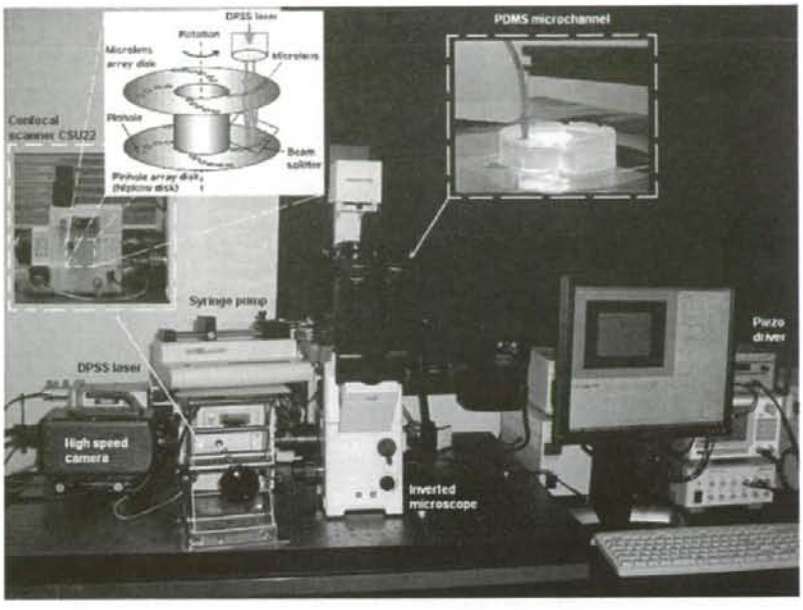

Fig. 4 Confocal micro-PIV experimental setup

temperature (25–27°C). All procedures in this experiment were carried out in compliance with the Ethics Committee on Clinical Investigation of Tohoku University.

2.3 Confocal micro-PIV experimental setup

The confocal micro-PIV system used in this study is shown in Fig. 4. A detailed description of the confocal system can be found elsewhere (Lima et al. 2006). In brief, the confocal system consisted of an inverted microscope (IX71; Olympus, Japan) combined with a confocal scanning unit (CSU22; Yokogawa, Japan), a diode-pumped solid-state (DPSS) laser (Laser Quantum, UK) with an excitation wavelength of 532 nm, and a high-speed camera (Phantom v7.1; Vision Research, USA). The laser beam was illuminated from the bottom of the microscope stage through a dry 20× objective lens with a numerical aperture (NA) of 0.75. The light emitted from the fluorescent tracers flowing within the microchannel passed through a color filter into the CSU22 scanning unit, where light was reflected by a dichromatic mirror onto a high-speed camera to record the PIV images.

The rectangular PDMS microchannel (300 μm wide, 45 μm deep, 10 mm long) was placed on the stage of an inverted microscope and using a syringe pump (KD Scientific, USA), a constant pressure-driven flow of 0.22 μl/min was maintained, corresponding to a Reynolds number (Re) of ~0.02 (based on the hydraulic diameter). A glass microsyringe (50 μl capacity) was used to obtain a flow rate as close as possible to a steady flow.

For the working fluids, PIV images were first captured with a resolution of 640 × 480 pixels, at a rate of 200 frames/s with an exposure time of 4995 μs and then recorded on a computer for evaluation using the Phantom camera control software (PH607). Using a dry 20×/0.75 NA objective lens, the estimated thickness of the measurement plane (optical slice thickness) was 4.97 μm. Moreover, using a high-speed

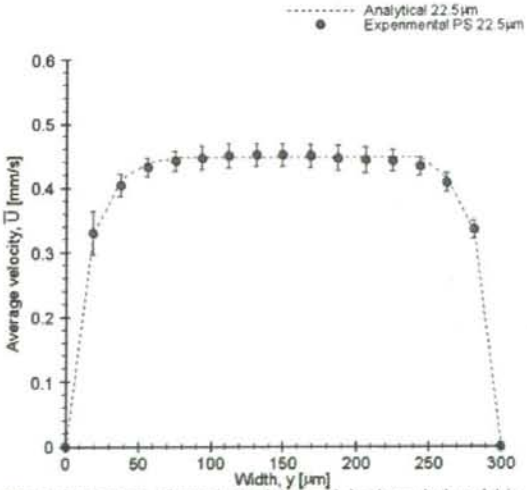

Fig. 5 Comparison of experimental data and the theoretical model in the central plane (22.5 μm). The *error bars* represent the standard deviation of six measurements using Student's *t* test with a 95% confidence interval

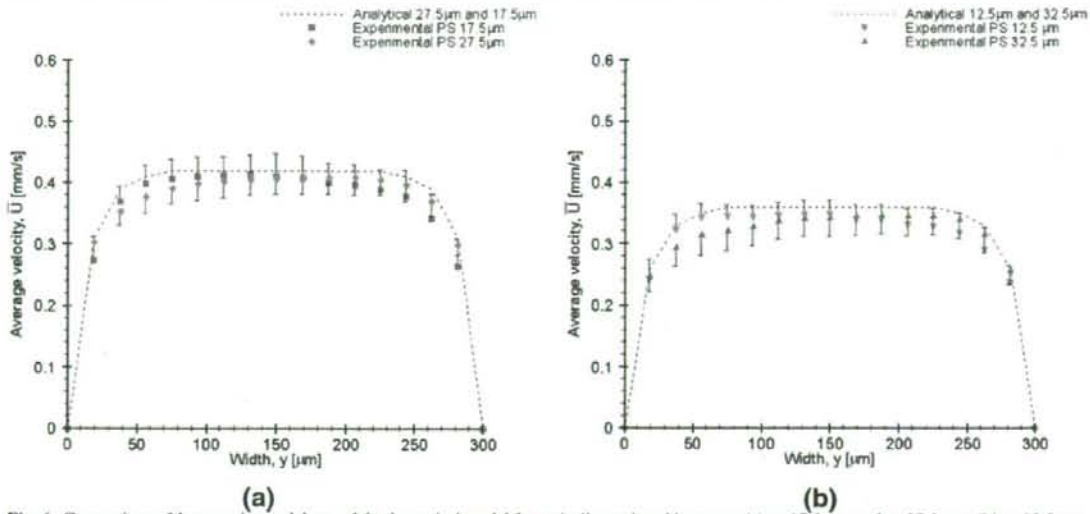

Fig. 6 Comparison of the experimental data and the theoretical model for optically sectioned images at (**a**) z=17.5 µm and z=27.5 µm; (**b**) z=12.5 µm and z=32.5 µm

objective lens actuator with submicron z-direction resolution it was possible to accurately capture optically sectioned images along the depth (z-axis) of the PDMS microchannel.

The PivView version 2.3 (PivTec, Germany) software (Willert et al. 1996; Raffel et al. 1998) was used to process the images by an iterative cross-correlation method (Willert et al. 1996; Raffel et al. 1998), while an advanced correlation technique (multi-grid interrogation) was used to improve the accuracy of the particle image displacement. The cross-correlation evaluation with grid refinement has been previously described (Willert et al. 1996; Raffel et al. 1998). In brief, the cross-correlation method is a statistical analysis that determines the average displacement by comparing the positions of the tracer particles within an interrogation area in two consecutive images. The cross-correlation function $R_{fg}(x, y)$ can be defined as (Raffel et al. 1998; Nguyen and Wereley 2002):

$$R_{fg}(x,y) = \sum_{i=1}^{p}\sum_{j=1}^{q} f(i,j)g(i+x,j+y), \tag{1}$$

where p and q are the dimensions (in pixels) of the interrogation area, and $f(i, j)$ and $g(i, j)$ represent the gray value distribution of the first and second image, respectively. The cross-correlation function correlates images of particles in two consecutive interrogation areas (particle image pair). The displacement of a particle image pair corresponds to the highest peak in the correlation plane. However, when small interrogation areas (usually less then 32 × 32 pixels) are used, random correlations can result in

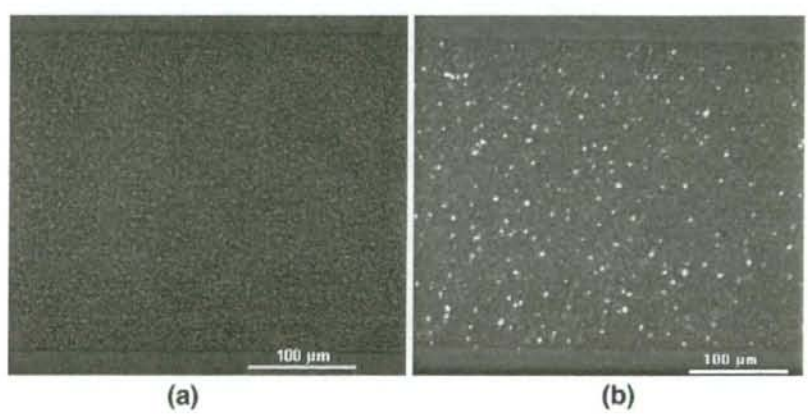

Fig. 7 (**a**) An image of *in vitro* blood (20% Hct) flow with halogen illumination. The RBCs are observed as dark grey rings. (**b**) Image of the same fluid in which both fluorescent particles and RBCs are visualised

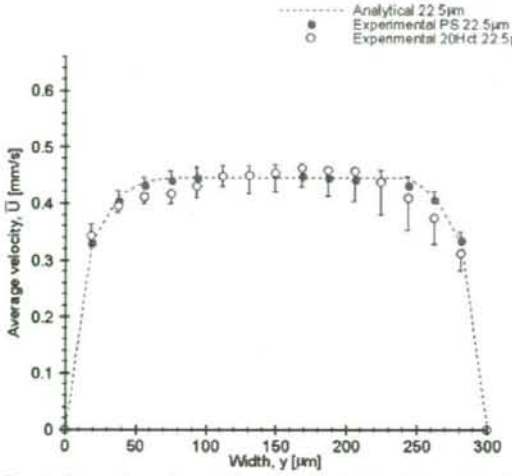

Fig. 8 Comparison of ensemble-averaged velocity of PS and *in vitro* blood in the central plane (22.5 μm)

noisy peaks and can generate an erroneous velocity vector (outlier). To reduce measurement uncertainty and to improve the signal-to-noise ratio, a multi-grid interrogation technique can be applied to the cross-correlation analysis (Raffel et al. 1998). The evaluation procedure of this advanced correlation technique is first based on a cross-correlation analysis at a relatively high correlation area (usually 32 × 32 pixels or more) to obtain an accurate estimate of the displacement and then the process is repeated at each pass by refining the interrogation area. By using this procedure, the displacement at a smaller interrogation area can be estimated with high accuracy, and consequently, high-resolution velocity vectors can be generated.

In our study, we used the iterative cross-correlation method, in which a multi-grid interrogation algorithm (grid refinement) was selected for evaluating the PIV image pairs. The initial interrogation area was 64 × 64 pixels whereas the final size was 24 × 32 pixel (50% overlap). Furthermore, the least squares Gauss fitting algorithm was used for detecting the peak on the correlation plane. Finally, the data were converted to the corresponding velocity fields using a magnification factor of 0.86 pixel/μm and pulse delay of 5 ms.

2.4 Ensemble averaged velocities

At steady flows, ensemble averaged velocities are known to improve the signal-to-noise ratio and consequently to generate more accurate velocity fields (Raffel et al. 1998; Meinhart et al. 2000). In this study, using the average velocity method, 100 instantaneous velocities measurements were ensemble-averaged to obtain the mean velocity field. This method first calculated the displacement field (peak detection) for each image pair and then the averaging operator was applied to all the instantaneous velocities measurements. The time-average mean velocity vector of the flow can be defined as

$$\vec{U} = \frac{\sum_{i=1}^{n} u_i}{n}, \tag{2}$$

where n is the number of valid instantaneous velocity measurements. In this study, we evaluated 100 images with time intervals of 5 ms.

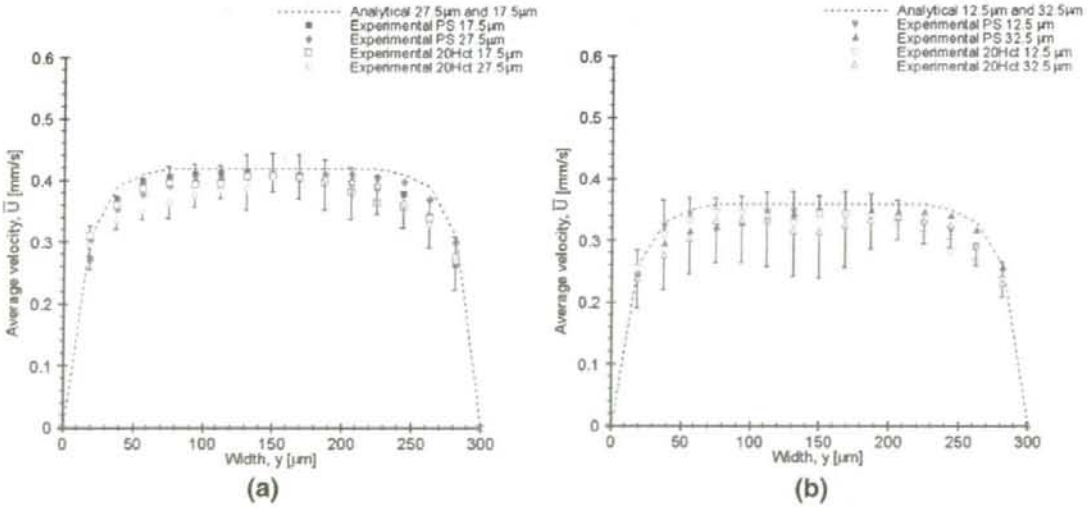

Fig. 9 Comparison of ensemble-averaged velocity of PS and *in vitro* blood at (**a**) z=17.5 μm and z=27.5 μm; (**b**) z=12.5 μm and z=32.5 μm

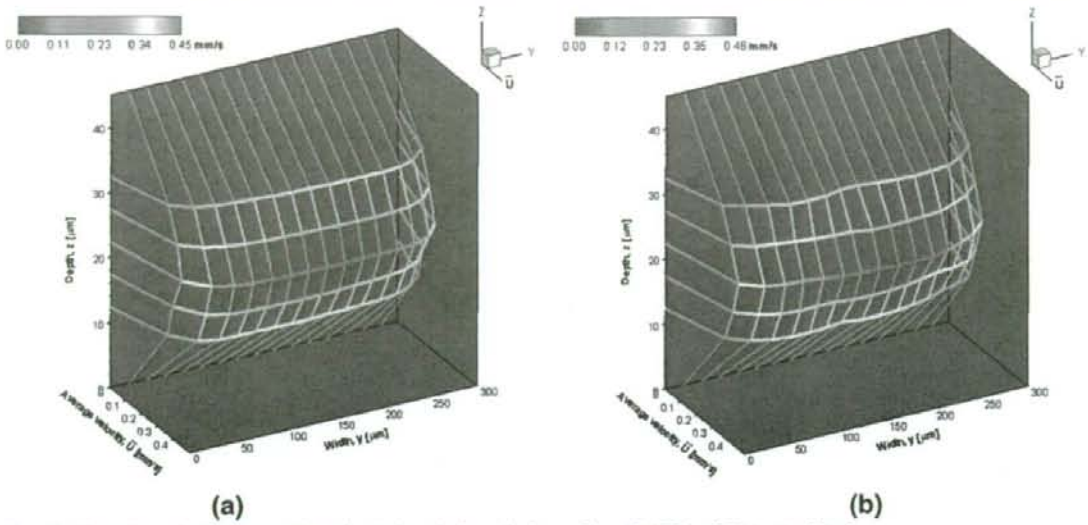

Fig. 10 Three-dimensional representation of optical sectioning velocity profiles of (**a**) PS and (**b**) *in vitro* blood

By calculating the u-component of the time-average mean velocity, it is possible to obtain the time-averaged velocity vector magnitude (U), which can be expressed as

$$U = \left|\overline{U}\right|. \tag{3}$$

The time-averaged velocity vector magnitude for six different samples ($\overline{U}$) was defined as

$$\overline{U} = \frac{1}{m \times n} \sum_{i=1}^{m} \sum_{i=1}^{n} U_i \tag{4}$$

where m is the number of samples used and n is the number of grid points along the x-direction.

3 Results

3.1 Physiological saline

To evaluate the performance of the confocal micro-PIV system in measuring the velocity fields of the working fluids through the PDMS rectangular microchannel, the experimental results for PS were compared to a well-established analytical solution for steady flow through a long, straight, rigid rectangular microchannel, that of Poiseuille flow. The equation used to calculate the analytical velocity profile of

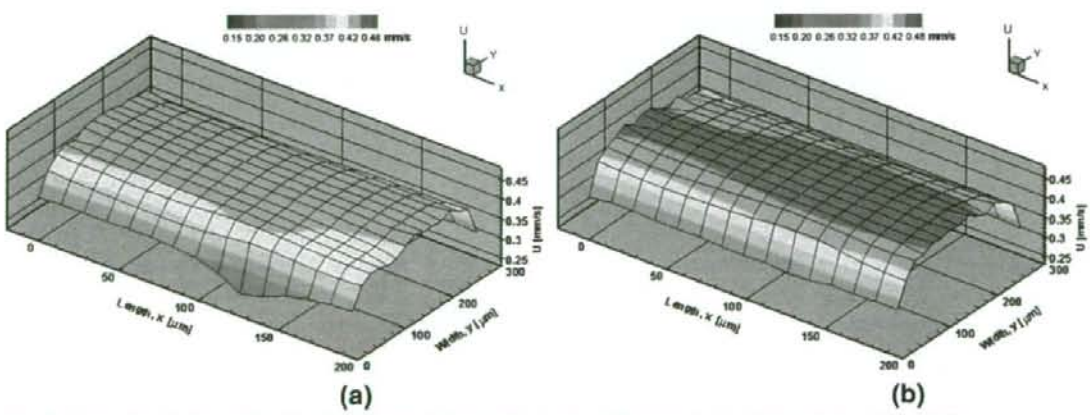

Fig. 11 Ensemble velocity profiles (U) of two representative samples in the middle plane for PS. (**a**) Sample 1 and (**b**) sample 2

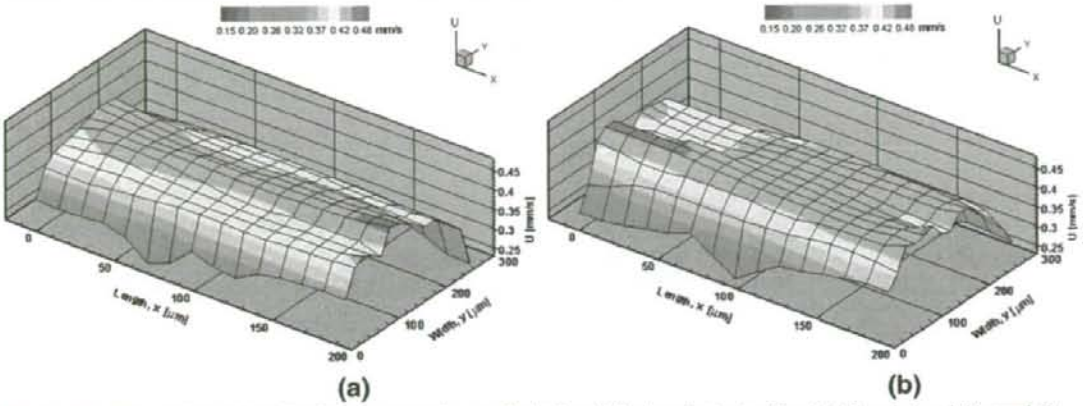

Fig. 12 Ensemble velocity profiles (U) of two representative samples in the middle plane for *in vitro* blood. (**a**) Sample 1 and (**b**) sample 2

the rectangular microchannel with y and z cross section is the following (Bruus 2004; Mortensen et al. 2005):

$$u_x(y,z) = \frac{48Q}{\pi^3 hw} \frac{\sum_{n,\text{odd}}^{\infty} \frac{1}{n^3}\left[1 - \frac{\cosh\left(n\pi\frac{y}{h}\right)}{\cosh\left(n\pi\frac{w}{2h}\right)}\right] \sin\left(n\pi\frac{z}{h}\right)}{\left[1 - \sum_{n,\text{odd}}^{\infty} \frac{192}{n^5\pi^5}\frac{h}{w} \tanh\left(n\pi\frac{w}{2h}\right)\right]}, \quad (5)$$

Fig. 13 Motion of one RBC flowing in a rectangular microchannel with a low aspect ratio (h/w=0.15). The RBC of interest has a *bright grey colour* in its central region. All images were captured with a 20× objective lens

where u_x is the fluid velocity in the x-direction, y and z are the directions normal to the flow, w and h are the width and depth of the microchannel, respectively, and Q is the flow rate.

Figures 5 and 6 compare the theoretical estimates using Eq. 5 and the average fluid velocities of 100 PIV image pairs for several optically sectioned planes along the microchannel depth. The PIV measurements were obtained with an exposure time of 4,995 μs, magnification factor (pixels/μm) of 0.86, and time interval of 5ms between two images.

Generally, the experimental results shown in Figs. 5 and 6 were in good agreement with the analytical solution, especially the results at the middle plane (z = 22.5 μm), where we found errors less than 5% (Fig. 5). As one moves out of the middle plane, the deviations start to increase and at locations close to the wall, the errors were about 7% (Fig. 6).

3.2 Blood flow

3.2.1 Ensemble-averaged velocity profiles

In addition to examining PS, we studied the behavior of *in vitro* blood (RBCs in PS, 20% Hct) through the rectangular PDMS microchannel. An example of a recorded image (halogen illumination source) of the *in vitro* blood flow is presented in Fig. 7(a). Figure 7(b) displays an image with both RBCs (halogen illumination) and fluorescent particles (laser-emitted light). The latter image could be used to calculate the velocity fields of the *in vitro* blood flow.

Figures 8 and 9 compare the mean velocity profiles of 100 ensemble image pairs for PS and *in vitro* blood (20% Hct), from six different measurements recorded at different x–y planes, spaced at 5-μm-depth intervals (z-direction). Both results were obtained under the same experimental conditions (Re = 0.02).

From Figs. 8 and 9, the velocity profiles of the PS fluid in several horizontal planes (x–y axis) clearly show that the

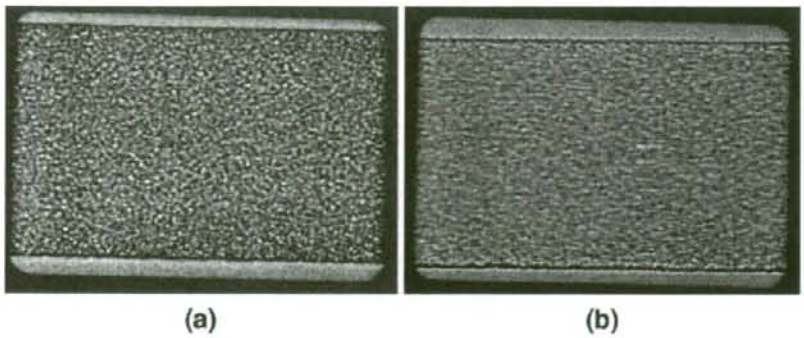

Fig. 14 Flow of RBCs (~20% Hct) suspended in PS through a rectangular PDMS microchannel 300 μm wide and 45 μm deep for a (**a**) Re ~0.02; (**b**) Re ~0.1

flow is stable and fully developed. In addition, Figs. 8 and 9 also show that for PS fluid, the shape of the mean velocity profile is markedly blunt in the middle region. However, examining the average velocity profiles of the *in vitro* blood, small deviations between the fluids were observed, especially in the regions near the walls. These small perturbations along the width of the microchannel become much clearer on analyzing the 3-D profiles shown in Fig. 10. Figure 10(a) indicates that the PS velocity profile along the z-direction had a smooth parabolic shape, whereas the *in vitro* blood flow (Fig. 10(b)) was characterized by a velocity profile containing several small disturbances along the z-direction.

3.2.2 Ensemble velocity profiles in the middle plane

It is generally agreed that the ensemble average velocity process improves the reliability and accuracy of PIV measurements because of the improvement in the signal-to-noise ratio and the reduction of measurement errors associated with the Brownian motion of the tracer particles and some possible "bottleneck" effects of the syringe pump. Furthermore, our experimental confocal PIV results with the PS fluid compared to the theoretical model (Fig. 5) showed the best agreement was in the middle plane of the microchannel (z = 22.5 μm) because of a reduction in several effects resulting from the microchannel wall (interaction between particle and wall, roughness of the wall, etc.). The PIV measurements in the middle plane seemed to generate results closer to the true velocity profile present in the rectangular PDMS microchannel. In this study, 6 samples of 100 PIV image pairs at the middle plane were analyzed for both PS and *in vitro* blood (~20% Hct). Figures 11 and 12 show the time-averaged velocity profiles (U) along a certain length (150 μm) from two different representative samples for PS and *in vitro* blood, respectively.

Figure 11 shows that when using PS fluid, a markedly smooth, flat profile tended to develop along the rectangular microchannel. However, for the *in vitro* blood flow, small perturbations in the shape of the ensemble velocity profiles were observed (Fig. 12). These qualitative observations can play an important role in providing reliable information on the time-averaged flow behavior over a specific period of interest.

3.2.3 RBC flow visualization

To determine possible causes of the perturbations in the velocity profiles of the *in vitro* blood flowing in the rectangular microchannel, RBC motion was visualized with halogen illumination from our confocal micro-PIV system. Figure 13 shows the dynamic behavior of the RBCs in a rectangular microchannel with a low aspect ratio. Figure 13

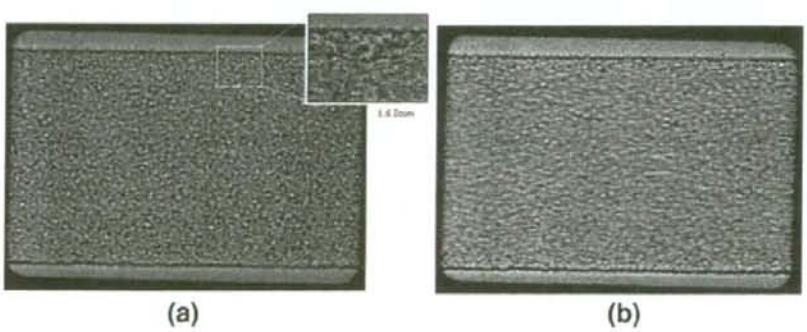

Fig. 15 Flow of RBCs (~20% Hct) suspended in dextran 40 (Dx-40) through a rectangular PDMS microchannel 300 μm wide and 45 μm deep for a (**a**) Re ~0.01; (**b**) Re ~0.08

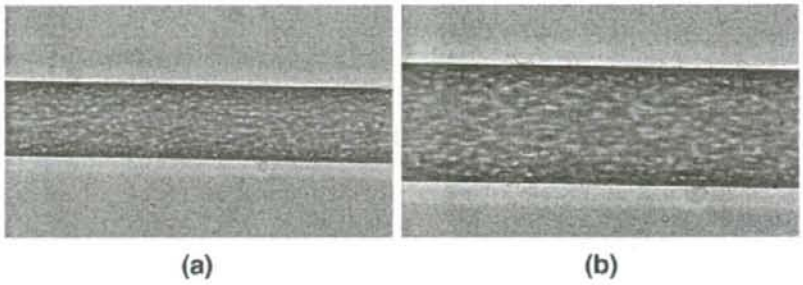

Fig. 16 Flow of RBCs (~20% Hct) suspended in dextran 40 (Dx-40) through a rectangular PDMS microchannel 100 μm wide and 62 μm deep for a Re of ~0.03 (**a**) 20× objective lens; (**b**) 32× objective lens

also shows detailed consecutive halogen images captured at time interyals of 10ms, when the motion of one particular RBC was followed.

During the capture of the images, we did not observe any significant plasma layer, but rather a homogeneous distribution of the RBCs. Furthermore, in the central region of the microchannel (shear rate close to zero), the RBCs tended to move along with the flow with a regular rotational motion, retaining their biconcave shape. Near to the wall, where the shear rate increases significantly, both rotational and tumbling motions accompanied by membrane deformation were observed (see detailed consecutive images in Fig. 13). Interactions between neighboring RBCs at different depth planes (boundary layers) were also observed along the full microchannel.

3.2.4 Plasma layer

The formation of a plasma-rich layer located between the RBC core and wall is well documented in glass microchannels with diameters less than 300 μm (Faharaeus and Lindqvist 1931; Chien et al. 1984; Maeda 1996; Pries and Secomb 2003). However, to our knowledge the effect of both geometry and suspension medium in a straight rectangular PDMS microchannel has not been investigated. In an effort to understand why we observed no plasma layer in our microchannel, first we investigated the effect of the flow rate on the formation of the plasma layer. Figure 14 shows *in vitro* blood (~20% Hct in PS) through the rectangular PDMS microchannel, for two different flow rates. The results illustrate that the RBCs flowing in this particular microchannel (300 μm wide, 45 μm deep) have no tendency to migrate toward the center axis for a Re of up to 0.1.

We next investigated the effect of the suspension fluid. In Fig. 15, we show human RBCs (~20% Hct) suspended in dextran 40 (Dx-40, Otsuka Medicine, Japan) for Re values up to 0.08. Using this high-molecular-weight suspension fluid, we eliminated the effects of sedimentation of the RBCs at low shear rates. The qualitative results from Fig. 15 also show no tendency for the RBCs to undergo axial migration.

Finally, we investigated the flow behavior of RBCs (~20% Hct) suspended in Dx-40 through a smaller PDMS microchannel (100 μm wide, 62 μm deep), for a Re of ~0.03 (see Fig. 16). In contrast to the previous results, the RBCs flowing through this PDMS microchannel had a tendency to migrate toward the microchannel axis, promoting the formation of a plasma layer. Although we do not have extensive data on the influence of the width, it is nevertheless clear that the formation of the plasma layer is enhanced as the width becomes narrower.

4 Discussion

4.1 Flow behavior of PS and *in vitro* blood through a PDMS microchannel

In the present study, we determined the velocity profiles of PS fluid and *in vitro* blood (20% Hct) in a rectangular PDMS microchannel with a low aspect ratio (h/w = 0.15) using a confocal micro-PIV system. In the case of PS fluid, our results were in good agreement with the analytical solution around the central plane (z = 17.5 μm, z = 22.5 μm, and z = 27.5 μm). However, at locations closer to the wall, the errors were slightly larger than 7%. We believe that these larger errors were primarily attributable to "second-order effects," such as the surface roughness of the wall and background noise generated from particles adhering on the wall (bias effect). Although it is important to consider the data from all planes, we believe that the best results from the confocal system were presented in the middle plane. These results also demonstrated that around the central region, PS velocity profiles were markedly blunt, which is consistent with the characteristic behavior of a Newtonian fluid through a rectangular microchannel with a low aspect ratio.

By comparing the averaged ensemble velocity profiles of PS fluid and *in vitro* blood flow, we observed small deviations at all optically sectioned planes. These deviations were found to be larger at locations closer to the wall. Furthermore, the ensemble velocity profiles at the central

plane for the *in vitro* blood were not characterized by a flat profile in the central region; rather, the profile had small perturbations. The reasons for these small perturbations are still not completely understood. However, from the visualization of the RBCs' motion through the rectangular microchannel, interactions between neighboring RBCs seem to be an important factor to take into account. The abrupt increase in the shear rate in the vicinity of the wall likely plays an important role in the local disturbance effects caused by both rotational and tumbling motion of deformable RBCs within the fluid flow. Moreover, temporal variation in the hematocrit could be another factor contributing to the perturbations described above. From the six measurements (Fig. 12 shows two of six) performed at the center plane at different time periods, all showed random perturbations on the averaged ensemble velocity profiles. This suggests that the transverse motion of the RBCs fluctuates over time, consequently affecting the local apparent viscosity of the fluid. Effects such as Brownian motion, microelectrohydrodynamics, and bottlenecks (Tabeling 2001; Nguyen and Wereley 2002) seem unlikely to contribute significantly to the perturbations found in the *in vitro* blood velocity profiles because such perturbations were small when compared to the PS fluid profiles measured under the same experimental conditions. The present results suggest that the presence of deformable RBCs suspended within the plasma flow plays an important role on the hydrodynamic disturbance effect seen on the *in vitro* blood velocity profiles. These observations are consistent with several other measurements performed in glass microchannels (Goldsmith and Turitto 1986; Alonso et al. 1995; Lima et al. 2007). Further studies to clarify the presence of these fluctuations on the ensemble velocity profiles need to be conducted, not only using microchannels that closely mimic actual human microvessels, but also using higher resolution objective lenses.

4.2 Plasma layer in a straight PDMS microchannel

It is well known that RBCs in microvessels less than 300μm wide (Faharaeus and Lindqvist 1931; Chien et al. 1984; Pries and Secomb 2003) tend to migrate toward the axis, pro-

Table 2 Major advantages of PDMS microchannels over glass capillaries

Physicochemical factors that affect blood flow behavior	Glass capillaries	PDMS microchannels	Comments
Ability to culture endothelial cells near to confluence	Complex in closed microchannels	Possible	Recently techniques have been developed to culture endothelial cells near to confluence in PDMS microchannels[a,b,c]. To our knowledge, no work has reported culture cells near to confluence in closed glass microchannels. This is only possible by using parallel plate flow chambers[d].
Mechanical properties, ultimate tensile stress (UTS), Young's elastic modulus (E)	Rigid material (UTS ~300 to 900 MPa[e], E ~70 Gpa[e])	Flexible material (UTS ~3.9 to 10.8 MPa[f], E ~0.75 MPa[g])	PDMS microchannels may be able to mimic the deformability of *in vivo* microvessels (UTS ~0.4 to 1.4 MPa[h], E ~2.5 MPa[i]). PDMS allows large deflections with small actuation forces[g].
Geometry of the flow channel	Any kind of geometry using photolithography, but limited in cross section, especially aspect ratio	Any kind of geometry	Presently, it has become possible to fabricate rectangular PDMS microchannels with complex geometries[j,k]. Fabrication of microchannels in PDMS is simple, rapid, and has high replication fidelity. In contrast, fabrication in glass increases the time, complexity, and cost of the fabrication process[l].

[a] Borenstein et al. 2002
[b] Shin et al. 2004
[c] Kaji et al. 2006
[d] Brown 2000
[e] Rika nenpyo 1996
[f] Mata et al. 2005
[g] Unger et al. 2000
[h] Holzapfel et al. 2005
[i] Steiger et al. 1989
[j] Shevkoplyas et al. 2003
[k] Lima 2007
[l] McDonald and Whitesides 2002.

moting the formation of a plasma layer adjacent to the vascular walls. In the present study, we used a PDMS microchannel with a width of 300 μm and depth 45 μm. For this particular microchannel, no plasma layer was observed during our experiments. To clarify the formation of the plasma layer in PDMS microchannels, we investigated the effect of different parameters on the formation of the plasma layer, including geometry, flow rate, and suspending media. Under similar conditions, our results showed that for a 300-μm-wide microchannel, no plasma layer was formed, whereas for a 100 μm width, a thin plasma layer was clearly observed. Thus, our qualitative results indicate that the geometry of PDMS microchannel is primarily responsible for the formation of the plasma layer. In addition, our results indicate that the plasma layer is enhanced as the width becomes narrower. This finding is consistent with a recent study on the flow of RBCs in model constrictions (Faivre et al. 2006).

4.3 PDMS versus glass microchannels

Several studies on blood flow in glass microchannels and in microvessels have yielded conflicting results with respect to flow resistance and deformability of RBCs (Pries et al. 1994; Suzuki et al. 1996). However, the observed *in vivo/in vitro* discrepancies have not yet been convincingly explained. One way to overcome the limitations of glass capillaries is the use of PDMS microchannels. PDMS microchannels differ from glass capillaries in several ways (see Table 2):

1. The permeability to gases, such as oxygen, is a unique advantage culturing living endothelial cells near to confluence (Borenstein et al. 2002; Shin et al. 2004) in closed microchannels, a task extremely difficult to achieve in glass capillaries. Recently, a cellular micropatterning technique based on an electrochemical method (Kaji et al. 2006) was used successfully to culture endothelial cells on the surfaces of PDMS microchannels;
2. PDMS is an elastomeric and biocompatible material. The typical ultimate tensile stress (UTS) for PDMS ranges from 3.9 to 10.8 MPa (Mata et al. 2005), whereas the Young's elastic modulus (E) has a value of ~0.75 MPa (Unger et al. 2000). The UTS and E of blood vessels have values from 0.4 to 1.4 MPa (Holzapfel et al. 2005) and ~2.5 MPa (Steiger et al. 1989), respectively. The UTS and E are PDMS-formulation-dependent. PDMS may be able to more closely mimic the geometric and structural properties of *in vivo* microvessels by adjusting the ratio of the cross-linker (curing agent) and the thickness of the wall;
3. Using PDMS, it is easy to replicate complex microvascular networks with submicron fidelity (McDonald et al. 2002; Shevkoplyas et al. 2003; Shin et al. 2004; Lima 2007);
4. Due to its spontaneous adhesion onto glass substrates, PDMS sealing does not need any complex bonding technique. Thus, PDMS microchannels in addition to offering optimum optical access for confocal systems can be reused several times because of its reversible bonding. Glass-to-glass sealing requires elaborate bonding processes, such as direct, thermal compression, or hydrofluoric bonding methods, which are time-consuming and need very careful processing to obtain an acceptable yield. Using bonding interlayers, such as silicon for anodic bonding, metal for fusion or eutectic bonding, and spin-on-glass for thermal compression bonding are other options; however, the interlayer also tends to be deposited in the microchannel. In addition, all of these bonding methods need flat, smooth, and clean surfaces, which require a clean room facility.
5. It is possible to integrate several functional components, such as heaters, micromixers, micropumps, microvalves, and temperature and pressure sensors into a PDMS device (Fujii 2002; Thorsen et al. 2002).
6. No need exists to use a refractive-index-matching liquid to minimize refraction from the walls. As a result, it is possible to use high magnification objective lenses (40×, 60×, 100×) with high NA, which typically have a working distance from 100 to 200 μm. Consequently it is possible to obtain images with much higher resolution.

In addition, using a soft lithography technique, it is possible to easily fabricate precise and reproducible rectangular microchannels at low cost because the master mold is reusable. A rectangular PDMS microchannel with a low aspect ratio seems to be appropriate for performing confocal micro-PIV measurements of *in vitro* blood with Hcts close to the actual *in vivo* Hct in the microcirculation. However, this geometry may not reflect the actual physiology of the microcirculation. Hence, very recently we successfully fabricated straight circular PDMS microchannels using a wire-casting technique (Lima 2007). The fabrication of circular PDMS microchannels with complex geometries remains a challenge. Borenstein and his coworkers (Borenstein et al. 2002, Shin et al. 2004) are developing a precise alignment technique to produce true cylindrical channels. However, the alignment procedure is complex, time-consuming, and the thickness of the two matching PDMS templates containing the semicircular microchannels may limit its practical application with confocal systems.

Despite the limitations of PDMS microchannels, it is clear that this kind of microdevice exhibits features closer to actual physiological conditions than glass capillaries. Although PDMS microdevices are promising for mimicking the *in vivo* microvascular environment, many chal-

lenges remain. First, current PDMS fabrication processes need improvement to produce precise circular microchannels with thin walls less than 200 μm to obtain accurate measurements by means of confocal systems. Second, PDMS collapsible microchannels need to be developed to mimic the deformability of blood vessels more closely. Finally, it is also important to evaluate whether current cell culture techniques used in PDMS microchannels create a microvascular environment that is closely representative of the *in vivo* situation.

4.4 Ongoing development

The *in vitro* research performed with classical glass microchannels has revealed several phenomena that occur in the microcirculation. Some examples are the Fahraeus effect and Fahraeus–Lindqvist effect (Chien et al. 1984). However, several recent studies on flow resistance (Pries et al. 1994) and RBC deformation (Suzuki et al. 1996) have shown quantitative differences between the results in microvessels and in glass microchannels. The reason for these differences still remains unclear. Glass microchannels differ from microvessels in several respects, such as elasticity and geometry of the microchannel and biological effect by the endothelial inner surface. We believe that the limitations encountered in using glass microchannels can be overcome by employing a PDMS microchannel (see Table 2). Nevertheless, before moving to a more elaborate PDMS microchannel, we must first clarify the flow behavior of blood in terms of a simple geometry similar to the one used in the present study. To fully exploit the potential of this combined system, we are working to develop a biochip to mimic the *in vivo* environment. By using an innovative cellular micropatterning technique based on an electrochemical method (Kaji et al. 2006), we expect to culture endothelial cells on the surfaces of the PDMS microchannel to near confluence. In addition, by combining this microdevice with the confocal system, we will be able to identify and quantitatively measure cellular and molecular events occurring between the blood cells and endothelium. As a longer-range goal, we believe that this ongoing research will lead to new insights into complicated microcirculation phenomena, such as the role of the glycocalyx on the blood flow behavior and the thrombogenesis process.

Because of their outstanding properties, rectangular PDMS microchannels are gaining popularity in biomedical research. In addition to providing the ability to investigate a variety of phenomena in the microcirculation (Takayama et al. 1999; Fujii 2002; Shevkoplyas et al. 2003), this kind of microfluidic device may be useful as a "lab-on-a-chip," a clinical diagnostic instrument. However, until now, precise measurements of blood flow behavior through this kind of microchannel have not been performed. In the present study, we demonstrated that by combining the rectangular PDMS microchannel with a confocal micro-PIV system it is possible to obtain both qualitative and quantitative information about the complex biophysical behavior of *in vitro* blood flow at a mesoscopic level. Thus, we believe that the present combination has potential as a powerful tool to investigate several phenomena in the microcirculation.

5 Conclusions

We applied a confocal micro-PIV system to examine PS and *in vitro* blood flowing in a rectangular PDMS microchannel with a low aspect ratio. For PS, the flattening of the velocity profiles was in good agreement with an established analytical solution for this kind of microfluidic device. However, when we assessed the flow of *in vitro* blood (20% Hct), small fluctuations were observed in the velocity profiles at optically sectioned planes along the z-axis. Blood flow measurements performed at the center plane of the microchannel clearly show small fluctuations on averaged ensemble velocity profiles. The reasons for the encountered "microturbulences" are not entirely clear, but our qualitative observations indicate that interactions between neighboring RBCs, the high shear rate generated in the vicinity of the walls, and temporal fluctuations in the hematocrit may play important roles in the hydrodynamic disturbance effects encountered in the blood velocity profiles. However, due to the variety of complex phenomena occurring at the microscale level, further studies are needed to clarify the presence of these fluctuations on the ensemble velocity profiles.

The measurements presented in this study clearly showed that confocal micro-PIV can be effectively integrated with a PDMS microchannel to obtain blood velocity profiles along the full depth of the microchannel because of its 3-D optical sectioning capability. This study also demonstrated that the combination of confocal micro-PIV systems with PDMS microchannels can play an important role in not only assessing existing theories, models, and computer simulations of the microcirculation, but also in the development of a more accurate biochip device for various biomedical applications, such as patient diagnosis and monitoring, drug delivery, and cancer cell detection.

Acknowledgements This study was supported in part by the following grants: International Doctoral Program in Engineering from the Ministry of Education, Culture, Sports, Science and Technology of Japan (MEXT), "Revolutionary Simulation Software (RSS21)" next-generation IT program of MEXT; Grants-in-Aid for Scientific Research from MEXT and JSPS Scientific Research in Priority Areas (768) "Biomechanics at Micro- and Nanoscale Levels," Scientific Research (A) No.16200031 "Mechanism of the formation, destruction, and movement of thrombi responsible for ischemia of vital organs".

The authors also thank all members of Esashi, Ono and Tanaka Lab. for their assistance in fabricating the PDMS microchannel.

References

R. Adrian, Annu. Rev. Fluid Mech. **23**, 261–304 (1991)

C. Alonso, A. Pries, O. Kiesslich, D. Lerche, P. Gaehtgens, Am. J. Physiol. **268**(1 Pt 2), H25–H32 (1995)

M. Baker, H. Wayland, Microvasc. Res. **7**, 131–143 (1974)

D. Beebe, G. Mensing, G. Walker, Annu. Rev. Biomed. Eng. **4**, 261–286 (2002)

L. Bitsch, L. Olesen, C. Westergaard, H. Bruus, H. Klank, J. Kutter, Exp. Fluids **39**, 505–511 (2005)

J. Borenstein, H. Terai, K. King, E. Weinberg, M. Kaazempur-Mofrad, J. Vacanti, Biomedical Microdevices **4**(3), 167–175 (2002)

G. Born, A. Melling, J. Whitelaw, Biorheology **15**, 163–172 (1978)

T. Brown, J. Biomech. **33**, 3–14 (2000)

H. Bruus, *Theoretical microfluidics* (MIC, Technical University of Denmark, Denmark, 2004)

G. Bugliarello, J. Hayden, Trans. Soc. Rheol. **7**, 209–230 (1963)

C. Caro, T. Pedley, R. Schroter, W. Seed, *The mechanics of the circulation* (Oxford University Press, 1978)

W. Chang, D. Akin, M. Sedlak, M. Ladisch, R. Bashir, Biomedical Microdevices **5**(4), 281–290 (2003)

S. Chien, S. Usami, R. Skalak, *Blood flow in small tubes Handbook of Physiology – The cardiovascular system IV* (1984) 217–249

T. Cochrane, J. Earnshaw, A. Love, Med. Biol. Eng. Comput. **19**, 589–596 (1981)

C. Duffy, J. McDonald, O. Schueller, G. Whitesides, Anal. Chem. **70**, 4974–4984 (1998)

S. Einav, R. Berman, P. Fuhro, P. DiGiovanni, S. Fine, J. Fridman, Biorheology **12**, 207–210 (1975)

R. Fahraeus, T. Lindqvist, Am. J. Physiol. **96**, 562–568 (1931)

M. Faivre, M. Abkarian, K. Bickraj, H. Stone, Biorheology **43**, 147–159 (2006)

T. Fujii, Microelectron. Eng. **61–62**, 907–914 (2002)

P. Gaehtgens, Biorheology **24**, 367–376 (1987)

P. Gaehtgens, H. Meiselman, H. Wayland, Microvasc. Res. **2**, 13–23 (1970)

S. Gifford, M. Frank, J. Derganc, C. Gabel, R. Austin, T. Yoshida, W. Bitensky, Biophys. J. **84**, 623–633 (2003)

H. Goldsmith, V. Turitto, Tromb. Haemost. **55**, 415–435 (1986)

H. Golster, M. Linden, S. Bertuglia, A. Colantuoni, G. Nilsson, F. Sjoberg, Microvasc. Res. **58**, 62–73 (1999)

R. Gomez, R. Bashir, A. Sarikaya, M. Ladish, J. Sturgis, J. Robison, T. Geng, A. Bhunia, H. Apple, S. Wereley, Biomedical Microdevices **3**(3), 201–209 (2001)

G. Holzapfel, G. Sommer, C. Gasser, P. Regitnig, Am. J. Physiol Heart Circ. Physiol. **289**, H2048–H2058 (2005)

H. Kaji, T. Kawashima, M. Nishizawa, Langmuir **22**, 10784–10787 (2006)

G.B. Kim, S.J. Lee, Exp Fluids **41**, 195–200 (2006)

H. Kinoshita, M. Oshima, S. Kaneda, T. Fujii, Proceedings of the 9thICMSCLS (Boston, Massachusetts, USA, 2005)

A. Koutsiaris, D. Mathioulakis, S. Tsangaris, Meas. Sci. Technol. **10**, 1037–1046 (1999)

R. Lima, Analysis of the blood flow behavior through microchannels by confocal micro-PIV/PTV system, Doctoral thesis (Tohoku University, Japan, 2007)

R. Lima, S. Wada, K. Tsubota, T. Yamaguchi, Proceedings of the 3rd IASTED ICB—BioMech (Benidorm, Spain, 485, 2005)

R. Lima, S. Wada, K. Tsubota, T. Yamaguchi, Meas. Sci. Technol. **17**, 797–808 (2006)

R. Lima, S. Wada, M. Takeda, K. Tsubota, T. Yamaguchi, J. Biomech. **40**, 2752–2757 (2007)

N. Maeda, Jpn. J. Physiol **46**, 1–14 (1996)

A. Mata, A. Fleischman, S. Roy, Biomedical Microdevices **7**(4), 281–293 (2005)

J. McDonald, G. Whitesides, Acc. Chem. Res **35**(7), 491–499 (2002)

G. Mchedlishvili, N. Maeda, Jpn. J. Physiol **51**, 19–30 (2001)

C. Meinhart, S. Wereley, J. Santiago, J. Fluids Eng **122**, 285–289 (2000)

G. Minas, J. Martins, J. Ribeiro, R. Wolffenbuttel, J. Correia, Sens. Actuators **110**, 33–38 (2004)

J. Moger, S. Matcher, C. Winlove, A. Shore, J. Biomed. Opt. **9**(5), 982–994 (2004)

N. Mortensen, F. Okkels, H. Bruus, Phys. Rev. E **71**, 1–4 (2005)

A. Nakano, Y. Sugii, M. Minamiyama, H. Niimi, Clin. Hemorheol. Microcirc. **29**, 445–455 (2003)

N. Nguyen, S. Wereley, *Fundamentals and applications of microfluidics* (Artech House, Inc., Norwood, MA, 2002)

J. Park, K. Kihm, Opt. Lasers Eng. **44**, 208–223 (2006)

J. Park, C. Choi, K. Kihm, Exp. Fluids **37**, 105–119 (2004)

A. Parthasarathi, S. Japee, R. Pittman, Ann Biomed. Eng. **27**, 313–325 (1999)

A. Pries, T. Secomb, Clin. Hemorheol. Microcirc. **29**, 143–148 (2003)

A. Pries, T. Secomb, T. Gessner, M. Sperandio, J. Gross, P. Gaehtgens, Circ. Res. **75**, 904–915 (1994)

M. Raffel, C. Willert, J. Kompenhans, *Particle image velocimetry: a practical guide* (Springer, Germany, 1998)

Rika nenpyo, Chronological scientific tables, (National Astronomical Observatory), Maruzen Co., Japan, 1996

J. Santiago, S. Wereley, C. Meinhart, D. Beebe, R. Adrian, Exp Fluids **25**, 316–319 (1998)

T. Secomb, Symp. Soc. Exp. Biol. vol 49 (London, UK, 1995), pp. 305–321

S. Shevkoplyas, S. Gifford, T. Yoshida, M. Bitensky, Microvasc. Res. **65**, 132–136 (2003)

M. Shin, K. Matsuda, O. Ishii, H. Terai, M. Kaazempur-Mofrad, J. Borenstein, M. Detmar, J. Vacanti, Biomedical Microdevices **6** (4), 269–278 (2004)

H. Steiger, R. Aaslid, S. Keller, H. Reulen, Heart Vessels **5**(1), 41–46 (1989)

N. Sutton, M. Tracey, I. Johnston, R. Greenaway, M. Rampling, Microvasc. Res. **53**, 272–281 (1997)

Y. Suzuki, N. Tateishi, M. Soutani, N. Maeda, Microcirculation **3**, 49–57 (1996)

P. Tabeling, Proceedings of the 14th Australasian Fluid Mechanics Conference (Adelaide, Australia, 2001)

S. Takayama, J. McDonald, E. Ostuni, M. Liang, P. Kenis, F. Ismagilov, G. Whitesides, Patterning cells and their environments using multiple laminar fluid flows in capillary networks Proc. Natl. Acad. Sci. **96**, 5545–5548 (1999)

T. Tanaani, S. Otsuki, N. Tomosada, Y. Kosugi, M. Shimizu, H. Ishida, Appl. Opt. **41**(22), 4704–4708 (2002)

G. Tangelder, D. Slaaf, M. Muijtjens, T. Arts, M. Egbrink, R. Reneman, Circ. Res. **59**, 505–514 (1986)

T. Thorsen, S. Maerkl, S. Quake, Science **298**, 580–584 (2002)

M. Toner, D. Irimia, Annu. Rev. Biomed. Eng. **7**, 77–103 (2005)

K. Tsukada, H. Minamitami, E. Sekizuka, C. Oshio, Physiol. Meas. **21** (4), 459–471 (2000)

W. Uijttewaal, E. Nijhof, R. Heethaar, J. Biomech. **27**, 35–42 (1994)

M. Unger, H. Chou, T. Thorsen, A. Scherer, S. Quake, Science **288**, 113–116 (2000)

P. Vennemann, K. Kiger, R. Lindken, B. Groenendijk, S. Stekelenburg-de Vos, T. Hagen, N. Ursem, R. Poelmann, J. Westerweel, B. Hierk, J. Biomech. **39**, 1191–1200 (2006)

S. Wilhelm, B. Grobler, M. Gluch, H. Heinz, *Confocal laser scanning microscopy: principles* (Carl Zeiss, Germany, 2003)

C. Willert, M. Raffel, J. Kompenhans, B. Stasicki, C. Kahler, Flow Meas. Instrum. **7**, 247–256 (1996)

Preparation of amine free silica-coated AgI nanoparticles with modified Stöber method

Y. Kobayashi[1,2]*, N. Shimizu[1], K. Misawa[1], M. Takeda[3], N. Ohuchi[3], A. Kasuya[4] and M. Konno[1]

In recent years, the authors studied on fabrication of silica-coated AgI (AgI–SiO_2) nanoparticles with a Stöber method toward new X-ray contrast agents. In the Stöber method, amines are often used as catalysts for silica formation, so that it is probable that amine is left in the silica-coated particles. Since amines are harmful to the human body, amine free particles are desired for medical use. From this viewpoint, amine free AgI–SiO_2 nanoparticles were prepared with a modified Stöber method using NaOH as a catalyst instead of amine in the present work. The AgI nanoparticles were prepared from $AgClO_4$ and KI with the use of 3-mercaptopropyltrimethoxysilane (MPS) as a silane coupling agent and NaOH catalyst for alkoxide hydrolysis. The silica-coating was performed at $4{\cdot}5 \times 10^{-5}$M MPS, 15–22·5M water, 0·0008–0·0024M NaOH and 0·0004–0·009M tetraethylorthosilicate at an AgI concentration of 0·001M. AgI–SiO_2 particles as small as ca. 30 nm could be successfully fabricated at the concentrations of $4{\cdot}5 \times 10^{-5}$M MPS, 20M water, 0·0011M NaOH, 0·001M AgI and 0·004M tetraethylorthosilicate.

Keywords: AgI, Nanoparticle, Core–shell, Silica coating, Sol–gel, Stöber method

Introduction

Iodine compounds have been used as X-ray contrast agents in the field of medicine,[1] because of their low transmittance property for X-ray. The iodine compounds may provoke adverse events as allergic reactions in patients,[1] so that they cannot be administered to such people. Core–shell nanoparticles are good candidates for prevention of allergic reactions, because the shell materials can keep the contrast agents from living systems.

Silica coating of metal naoparticles has been intensively studied by Liz-Marzán *et al.*[2] Giersig *et al.* extended the silica-coating technique to fabrication of silica coated AgI nanoparticles, which employed a reaction of silica-coated Ag nanoparticles with I_2 for formation of AgI.[3]

The authors proposed an alternative method for silica-coating of an iodine compound AgI with a Stöber method,[4–6] and obtained silica coated AgI nanoparticles contrast agents for X-ray computed tomography.[7] However, in the Stöber method, amines are often used as catalysts for silica formation,[8] so that it is probable that amine is left in the silica-coated particles. Since amines are harmful to the human body,[9,10] amine free particles are desired for medical use. For producing amine free silica-coated AgI nanoparticles, the present work proposes a modified method using NaOH as the catalyst instead of amine.

[1]Department of Chemical Engineering, Graduate School of Engineering, Tohoku University, Aoba, Aramaki-aza, Aoba-ku, Sendai 980-8579, Japan
[2]Department of Biomolecular Functional Engineering, Faculty of Engineering, Ibaraki University, 4-12-1 Nakanarusawa-cho, Hitachi, Ibaraki 316-8511, Japan
[3]Division of Surgical Oncology, Graduate School of Medicine, Tohoku University, Seiryo-machi, Aoba-ku, Sendai 980-8574, Japan
[4]Centre for Interdisciplinary Research, Tohoku University, Aoba, Aramakiaza, Aobaku, Sendai 980-8578, Japan

*Corresponding author, email ykoba@mx.ibaraki.ac.jp

Experimental

Chemicals

$AgClO_4$ (Kanto Chemical Co., Inc., 99%) and KI (Wako Pure Chemicals Ltd, 99·5%) were used as AgI precursors. Tetraethylorthosilicate (TEOS) (Wako Pure Chemicals Ltd, 95%), 3-mercaptopropyltrimethoxysilane (MPS) (Aldrich, 97%) and ethanol (Wako Pure Chemicals Ltd, 99·5%) were used for silica coating, and sodium hydroxide (NaOH) (Wako Pure Chemicals Ltd, 0·1M) was used as a catalyst for a sol–gel reaction of TEOS and MPS. All chemicals were used as received. Ultrapure deionised water (resistivity higher than 18 MΩ cm) was used in all the preparations.

Preparation of materials

Colloids of AgI nanoparticles were prepared by mixing of $AgClO_4$ and KI solutions at a constant Ag/I molar ratio of 1 : 2, as follows. A freshly prepared 2M $AgClO_4$ aqueous solution (0·015 mL) was added to 0·05M KI aqueous solution (6 mL) under vigorous stirring at room temperature to provide an AgI concentration of 5×10^{-3}M. Immediately after the mixing, colour of the solution turned yellow. The Stöber method with TEOS was applied to silica-coating of the AgI nanoparticles. To the AgI colloid was added an aqueous MPS solution. After 15 min, ethanol and TEOS were successively

Published by Maney on behalf of the Institute
Received 21 December 2007; accepted 14 March 2008
DOI 10.1179/174329408X315409

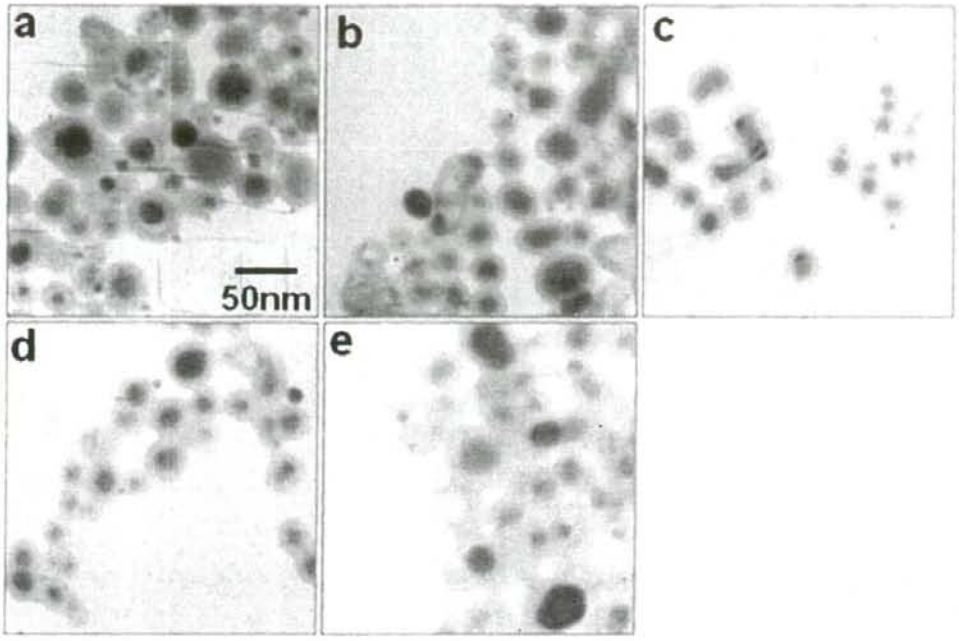

1 Images (TEM) of AgI–SiO_2 particles prepared at NaOH concentrations of *a* 0·0008, *b* 0·0009, *c* 0·001, *d* 0·0011 and *e* 0·0012M: initial concentrations of $AgClO_4$, KI, MPS, H_2O and TEOS were $1·0\times10^{-3}$, $2·0\times10^{-3}$, $4·5\times10^{-5}$, 20 and 0·004M with respect to total solution volume

added to the colloid. Then, the silica-coating was initiated by rapidly injecting an aqueous NaOH solution into the AgI/TEOS colloid. Initial concentrations of NaOH, H_2O and TEOS were varied from 0·0008 to 0·0024M, from 15 to 22·5M and from 0·0004 to 0·009M respectively, while initial concentrations of $AgClO_4$, KI and MPS were 0·001, 0·002 and $4·5\times10^{-5}$M respectively.

Characterisation

The AgI–SiO_2 particles were characterised by transmission electron microscopy (TEM) with a Zeiss LEO 912 OMEGA operating at 100 kV. Samples for TEM were prepared by dropping and evaporating the nanoparticle suspensions on a collodion coated copper grid. Silica shell thickness was estimated as the difference between AgI particle and composite particle sizes. Ultraviolet-visible (UV-VIS) extinction spectra were measured with a Hitachi UV-3010 spectrophotometer. X-ray diffraction (XRD) measurements were made with a Rigaku RU-200A diffractometer at 40 kV and 30 mA with Cu K_α radiation.

Results and discussion

Effect of NaOH concentration

Figure 1 shows the TEM images of AgI–SiO_2 particles prepared at various NaOH concentrations. At concentrations of 0·0008 and 0·0009M, shell free AgI nanoparticles were obtained due to a shortage of NaOH catalyst, though some silica coated AgI particles were also prepared. At 0·0010 and 0·0011M, the AgI nanoparticles were well coated with silica. Addition of NaOH probably increased the ionic strength of the solution. Thus, the increased ionic strength should reduce the double layer repulsion between the AgI nanoparticles and the silica nuclei. As a result, the silica nuclei were efficiently deposited on the AgI particle surfaces. When an NaOH concentration increased to 0·0012M, AgI cores in the AgI–SiO_2 particles became large. The further increased ionic strength would promote both aggregation and growth of AgI cores before silica coating. Besides, aggregation of the AgI–SiO_2 particles was observed. The increased ionic strength also provided the particle aggregation after silica-coating.

Effect of H_2O concentration

Figure 2 shows the TEM images of AgI–SiO_2 particles prepared at various H_2O concentrations. At concentrations of 20 and 22·5M, quasi-perfect core–shell structure was formed. Core–shell particles were also produced for concentrations as low as 15 and 17·5M. Compared to the high H_2O concentrations, the AgI cores were large. Because the dielectric constant of water/ethanol solution is low at low H_2O concentration, silanol groups on the surface of MPS modified AgI particles probably tend to deionise in the water/ethanol solution. Thus, the electrostatic repulsion between the AgI particles was weak, and thereby the AgI nanoparticles aggregated and grew in the water/ethanol solution before silica-coating. In addition, coalescence of the AgI–SiO_2 particles was observed. The low dielectric constant also provided deionisation of silanol groups on the surface of

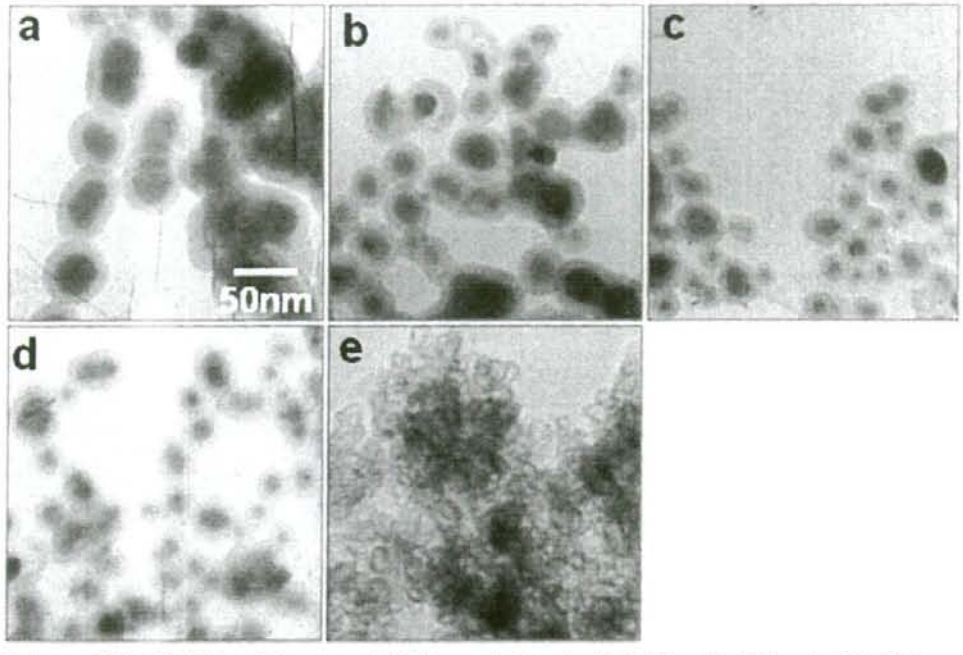

2 Images (TEM) of AgI–SiO_2 particles prepared at H_2O concentrations of *a* 15, *b* 17·5, *c* 20, *d* 22·5 and *e* 25M: initial concentrations of $AgClO_4$, KI, MPS, NaOH and TEOS were $1{\cdot}0\times10^{-3}$, $2{\cdot}0\times10^{-3}$, $4{\cdot}5\times10^{-5}$, 0·0011 and 0·004M with respect to total solution volume

AgI–SiO_2 particles. Consequently, the coalescence took place with a similar mechanism to the formation of large AgI cores. For a concentration as high as 25M, many secondary silica particles were produced. In contrary to the low H_2O concentration, the high H_2O concentration probably provides ionisation of silanol groups on the silica particle surface. Thus, the electrostatic repulsion between generated particles also increased. Therefore, silica nuclei generated during the early stages of the sol–gel reaction probably grew as stable secondary silica particles rather than on the existing cores.

Effect of TEOS concentration

Figure 3 shows the TEM images of AgI–SiO_2 particles prepared at various TEOS concentrations. At the concentrations of 0·0004 and 0·001M (Figs. 3*a* and *b*), no core–shell structure was formed, though a few core–shell particles were also produced for 0·001M. This result indicated that the amount of TEOS was not enough to coat AgI nanoparticles. For 0·004–0·009M (Figs. 3*c–f*), most of the particles were quasi-perfect core–shells with just one AgI core with a size ~20 nm. An average size of the AgI–SiO_2 particles was varied from 28·3 to 32·2 nm with the increase in TEOS concentration from 0·004 to 0·009M.

Ultraviolet-visible spectroscopy

Figure 4 gives the absorption spectrum of AgI–SiO_2 particle colloid. A sharp peak ~421 nm and a shoulder peak ~330 nm were observed, which were attributed to exciton peaks of AgI.[11–14] Thus, the existence of AgI nanoparticles was confirmed from the UV-VIS spectroscopy.

X-ray diffraction

Figure 5 shows the XRD pattern of AgI–SiO_2 particles. Peaks were observed at 22·4, 23·7, 25·4, 32·8, 39·2, 42·7 and 46·4°. Although these peaks were all attributable to β-AgI,[14] all peaks of γ-AgI overlap with the peaks of 002 (23·7°), 110 (39·2°) and 112 (46·4°) of β-AgI. Accordingly, the XRD measurement revealed that the obtained AgI nanoparticles were β-AgI or a mixture of β-AgI and γ-AgI.

Conclusion

AgI–SiO_2 particles were prepared by employing a sol–gel reaction of TEOS with NaOH catalyst in the presence of MPS modified AgI nanoparticles for producing AgI–SiO_2 particle colloid. Concentration effects of NaOH, H_2O and TEOS can probably be explained by the differences of the solution in dielectric constant and ionic strength. The coating reaction at $4{\cdot}5\times10^{-5}$M MPS, 20 M H_2O, 0·0011M NaOH, 0·001M AgI and 0·004–0·009M TEOS provided formation of AgI–silica core–shell structure that had sizes of ca. 30 nm.

Acknowledgement

This research was partially supported by the Ministry of Education, Culture, Sports, Science and Technology of

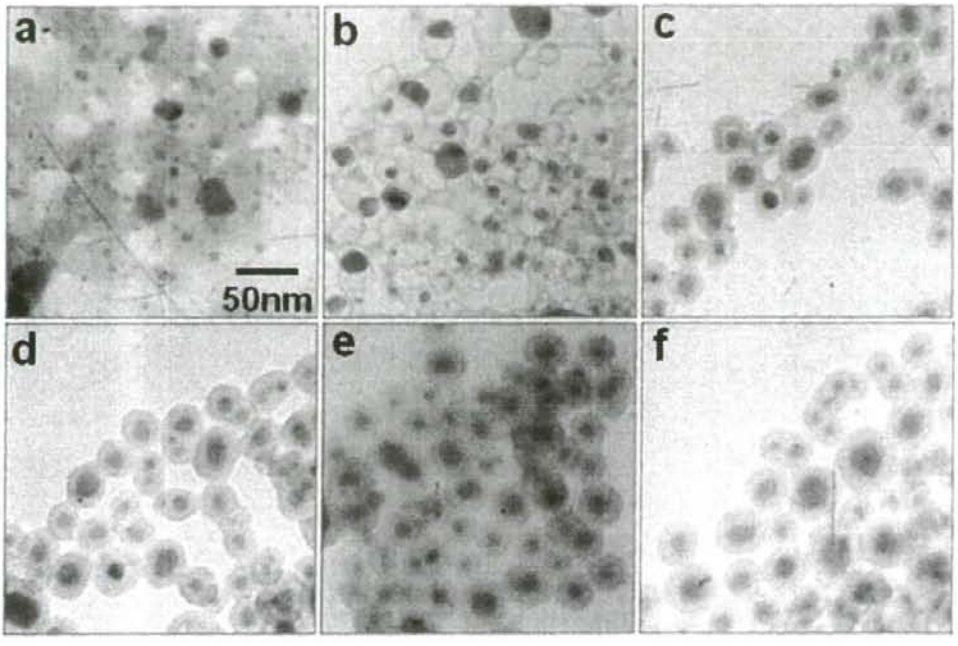

3 Images (TEM) of AgI–SiO_2 particles prepared at TEOS concentrations of *a* 0·0004, *b* 0·001, *c* 0·004, *d* 0·006, *e* 0·008 and *f* 0·009M: initial concentrations of $AgClO_4$, KI, MPS, H_2O and NaOH were $1·0\times10^{-3}$, $2·0\times10^{-3}$, $4·5\times10^{-5}$, 20 and 0·0011M with respect to total solution volume

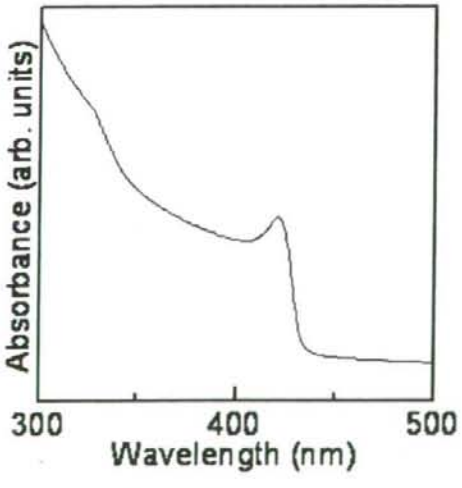

4 Ultraviolet-visible absorption spectrum of AgI–SiO_2 particle colloid: initial concentrations of $AgClO_4$, KI, MPS, H_2O NaOH and TEOS were $1·0\times10^{-3}$, $2·0\times10^{-3}$, $4·5\times10^{-5}$, 20, 0·0011 and 0·008M with respect to total solution volume

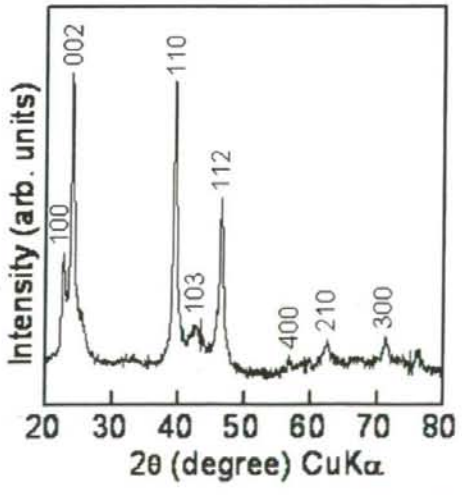

5 X-ray diffraction pattern of AgI–SiO_2 particles: initial concentrations of $AgClO_4$, KI, MPS, H_2O NaOH and TEOS were same as Fig. 4

Japan (Grant-in-Aid for the COE project, Giant Molecules and Complex Systems), and by the Ministry of Health, Labour and Welfare of Japan.

References

1. A. Joubert, M.-C. Biston, C. Boudou, J.-L. Ravanat, T. Brochard, A.-M. Charvet, F. Estève, J. Balosso and N. Foray: *Int. J. Radiat Oncol. Biol. Phys.*, 2005, **62**, 1486–1496.